



Lattice distortion and stability of $(\text{Co}_{0.2}\text{Cu}_{0.2}\text{Mg}_{0.2}\text{Ni}_{0.2}\text{Zn}_{0.2})\text{O}$ high-entropy oxide under high pressure

HPSTAR
1078-2020



B. Cheng^{a,b}, H. Lou^a, A. Sarkar^{d,e}, Z. Zeng^a, F. Zhang^d, X. Chen^a, L. Tan^a, K. Glazyrin^f, H.-P. Iiermann^f, J. Yan^{g,h}, L. Wangⁱ, R. Djenadic^{d,j}, H. Hahn^{d,e}, Q. Zeng^{a,c,*}

^a Center for High Pressure Science and Technology Advanced Research, Pudong, Shanghai 201203, People's Republic of China

^b Shanghai Institute of Laser Plasma, Shanghai, 201800, People's Republic of China

^c Jiangsu Key Laboratory of Advanced Metallic Materials, School of Materials Science and Engineering, Southeast University, Nanjing 211189, People's Republic of China

^d Joint Research Laboratory Nanomaterials, Technische Universität Darmstadt and Karlsruhe Institute of Technology, 64287 Darmstadt, Germany

^e Institute of Nanotechnology, Karlsruhe Institute of Technology, 76344 Eggenstein-Leopoldshafen, Germany

^f Photon Sciences, Deutsches Elektronen Synchrotron (DESY), Hamburg, Germany

^g Advanced Light Source, Lawrence Berkeley National Laboratory, Berkeley, CA 94720, USA

^h Department of Earth and Planetary Sciences, University of California, Santa Cruz, CA 95064, USA

ⁱ School of Materials Science and Engineering, Beijing Institute of Technology, Beijing 100081, People's Republic of China

ARTICLE INFO

Article history:

Received 15 May 2020

Accepted 25 June 2020

Available online xxx

Keywords:

Phase transition

Synchrotron x-ray diffraction

Pair distribution function

Nanocrystalline

ABSTRACT

High-entropy oxides (HEOs) stabilize multiple cations in a single solid solution phase, providing a new opportunity for property engineering in almost infinite compositional space. The structural stability and tunability of HEO are of great interest and importance but has not been well understood, especially under pressure. Here, we studied the structure evolution of a rock salt phase $(\text{Co}_{0.2}\text{Cu}_{0.2}\text{Mg}_{0.2}\text{Ni}_{0.2}\text{Zn}_{0.2})\text{O}$ HEO using *in situ* synchrotron X-ray diffraction, pair distribution function, Raman spectroscopy up to ~ 43 GPa, and *ex situ* transmission electron microscopy, a pressure-induced reversible rock salt to highly distorted cubic phase transition was observed. These results suggest highly tunable lattice distortion in HEOs under pressure, which could promote the fundamental understanding and also guide applications of HEOs.

© 2020 The Author(s). Published by Elsevier Ltd. This is an open access article under the CC BY-NC-ND license (<http://creativecommons.org/licenses/by-nc-nd/4.0/>).

1. Introduction

Over the centuries, materials development is mainly based on one principal element with a minor addition of other elements to meet the needs of designed properties. Therefore, traditional materials limit themselves mainly around the corner of multicomponent phase diagrams to avoid the formation of useless complex mixtures. In 2004, this materials development protocol was reformed by two independent pioneering works of Yeh et al. [1] and Cantor et al. [2], which report the formation of a single solid solution phase with multiple principal elements (usually five or more with equal or near-equal atomic ratio) randomly distributed on a simple crystalline lattice, so-called high-entropy alloys (HEAs).

Maximized configurational entropy is realized by the equal or near equal atomic ratio in compositions and is proposed to play an important role to stabilize complex compositions in a single lattice, opening an almost infinite composition space for new alloys exploration. Moreover, HEAs show great mechanical properties compared to traditional metallic materials [1–5]. Further, this high-entropy strategy has been successfully extended in many other material systems, including oxides in both bulk or nano forms [6].

Rost et al. synthesized the first high-entropy oxide (HEO) with a complex composition of $(\text{Mg}_{0.2}\text{Co}_{0.2}\text{Ni}_{0.2}\text{Cu}_{0.2}\text{Zn}_{0.2})\text{O}$ and a single rocksalt-type structure [7]. Subsequently, various types of HEOs have been explored, e.g. CaF_2 type [8], perovskites type [9–11], spinels type [12], and even amorphous type [13,14]. Due to the great flexibility for element-based property design and engineering, HEOs have attracted extensive attention as their tremendous potential in various applications. The reported remarkable properties of HEOs includes huge dielectric constant [15] and high room temperature Li-ion conductivity [16], which have advanced several

* Corresponding author.

E-mail address: zengqs@hpstar.ac.cn (Q. Zeng).

^j Present address: Heraeus Deutschland GmbH & Co. KG, Heraeusstr. 12–14, 63450 Hanau, Germany.

potential applications like defect dipoles [17], epitaxial interface engineering [18] and electrode materials in Li-ion battery [19,20].

High configurational entropy is evidenced to favor a single solid solution oxide phase at high enough temperatures in Gibbs free energy against multiphase oxides. Annealing below a critical high temperature could transform the single-phase HEOs back to their multiphase states and vice versa on heating. However, HEOs could be quenched to room temperatures and remains stable due to high energy barriers and low diffusion. Meanwhile, although HEO could form in a single phase, its lattice is believed to inevitably involve local distortion caused by different atomic radii of cations and oxygen vacancies. Considering the competing effects on the system free energy of high entropy (lowering) and lattice distortion (raising), the structure of HEOs could be highly tunable by imposed external parameters such as pressure. However, no much work has been done yet on the structural stability and tunability of HEOs under pressure, which remains an open field.

For HEAs, pressure-induced irreversible *fcc* to *hcp* polymorphic transitions were observed in the CoCrFeMnNi HEA [21–23] and a medium-entropy NiCoCrFe alloy [24], which confirms the existence of polymorphism in high-entropy materials. More complex transitions of *hcp* → Sm-type → *dhcp* → *dfcc* were further reported in an *hcp*-structured HoDyYGdTb HEA [25]; even five polymorphs were discovered in the *bcc* Al_{0.6}CoCrFeNi HEA [26,27]. These results show rich polymorphic phenomena in HEAs and suggest general structural tunability may exist in high-entropy materials [28]. In the case of HEOs, besides the contribution of pressure as the pressure-volume (*PV*) work to the Gibbs energy ($G = U + PV - ST$), the local lattice distortion, high-level oxygen vacancies, and even electronic states (valency) are all expected to be susceptible to pressure tuning. Recently, a pressure-induced amorphization at room temperature has been found in a (Ce_{0.2}La_{0.2}Pr_{0.2}Sm_{0.2}Y_{0.2})O_{2-δ} nano-HEO as a consequence of continuous tuning of lattice distortion under high pressure [14]. In contrast, no obvious structural transition was reported by Chen et al. in undoped and Li/Mn-doped (Co_{0.2}Cu_{0.2}Mg_{0.2}Ni_{0.2}Zn_{0.2})O up to ~50 GPa [29]. These results cause more confusion about the stability of the HEOs lattice, which calls for further work to clarify it.

Herein, we combined *in situ* high-pressure synchrotron X-ray diffraction (XRD), pair distribution function (PDF), and optical laser Raman spectroscopy in diamond anvil cells (DACs) to investigate the structural evolution of the prototype transition metal (Co_{0.2}Cu_{0.2}Mg_{0.2}Ni_{0.2}Zn_{0.2})O HEO (TM-HEO). The interplanar *d*-spacings, bond length, and bond angles were carefully determined to monitor the lattice stability and distortion during compression up to ~43 GPa. Although no symmetry breaking, the rock salt lattice of the TM-HEO becomes obviously distorted above ~9 GPa, which further suggests the generality of high tunability of lattice distortion in HEOs.

2. Experimental section

2.1. Sample synthesis and characterization

(Co_{0.2}Cu_{0.2}Mg_{0.2}Ni_{0.2}Zn_{0.2})O TM-HEO nanocrystalline powder samples were synthesized using nebulized spray pyrolysis method [30]. The powders have a small average grain size of ~44 nm, but fine grains aggregate into hollow spheres with a broad particle size distribution. The structure of the initial TM-HEO sample at ambient conditions was characterized by synchrotron high-energy XRD.

2.2. Synchrotron XRD measurements

High-energy XRD experiments were performed at the beamline 11-ID-C at Advanced Photon Source (APS), Argonne National Laboratory (ANL) with an X-ray wavelength of 0.1173 Å and a beam size of 0.5 × 0.5 mm². The exposure time was set to 60 s. The two-dimensional (2D) diffraction images were collected by a Perkin-Elmer amorphous *a*-Si detector, with a maximum wave vector momentum transfer of $q \approx 30 \text{ \AA}^{-1}$. *In situ* high-pressure angle-dispersive XRD experiments were mainly performed at the beamline P02.2, PETEA-III, Desy, Germany [31]. A monochromatic X-ray beam with a wavelength of 0.2895 Å was focused by a Kirkpatrick-Baez (KB) mirror system down to approximately 7.7 × 3.3 μm² at the rotation center of the sample stage. XRD signal was collected by a 2D Perkin-Elmer amorphous *a*-Si detector, with a maximum wave vector momentum transfer of $q \approx 16 \text{ \AA}^{-1}$. The position and orientation of the detector to the X-ray beam were calibrated using the diffraction pattern of a CeO₂ standard. High pressure was generated using a symmetric DAC [32] with a culet size of ~300 μm in diameter. The gasket was rhenium that was preindented to ~20 GPa. A hole with a diameter of ~120 μm was drilled to serve as the sample chamber by a laser drilling system at the center of the gasket indent. The TM-HEO powder was prepressed into a thin pellet and cut into flakes with proper sizes for DACs. Then, a tiny flake was loaded into a DAC along with a tiny ruby ball and Au foil beside the sample to calibrate pressure. Methanol: ethanol = 4:1 (volume ratio) mixture was used as the pressure-transmitting medium. The background scattering was collected at each pressure point by shining the X-ray beam on the empty area inside the sample chamber, which only passed through the pressure medium and two diamond anvils. The exposure time was set to 10 s and accumulated 10 times for better statistics. One-dimensional (1D) XRD patterns were obtained by integrating the 2D images along the azimuth angle from 0° to 360° with the Dioptas software [33]. The resulting diffraction patterns were refined using the GSAS package, and the structure factors $S(q)$ and reduced PDF $G(r)$ were obtained using the PDFgetX3 package [34]. Repeated *in situ* high-pressure angle-dispersive XRD experiments using DACs with different pressure mediums such as neon and silicone oil were conducted at the beamline 13-ID-D, APS, ANL, the beamline 12.2.2 at Advanced Light Source (ALS) in Lawrence Berkeley National Laboratory

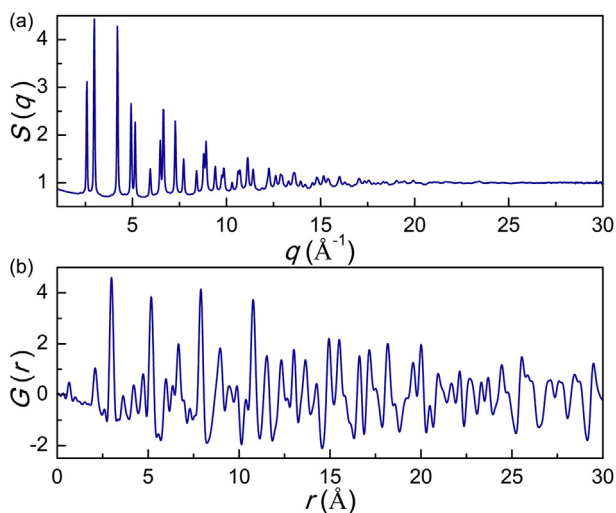


Fig. 1. Structure factor and pair distribution function of the initial sample. The structure factor $S(q)$ (a) and pair distribution function $G(r)$ (b) of the (Co_{0.2}Cu_{0.2}Mg_{0.2}Ni_{0.2}Zn_{0.2})O TM-HEO at ambient conditions obtained by high-energy XRD. The X-ray wavelength was 0.1173 Å. A transmission mode was used for the sample without any container. HEO, high-entropy oxide; XRD, X-ray diffraction.

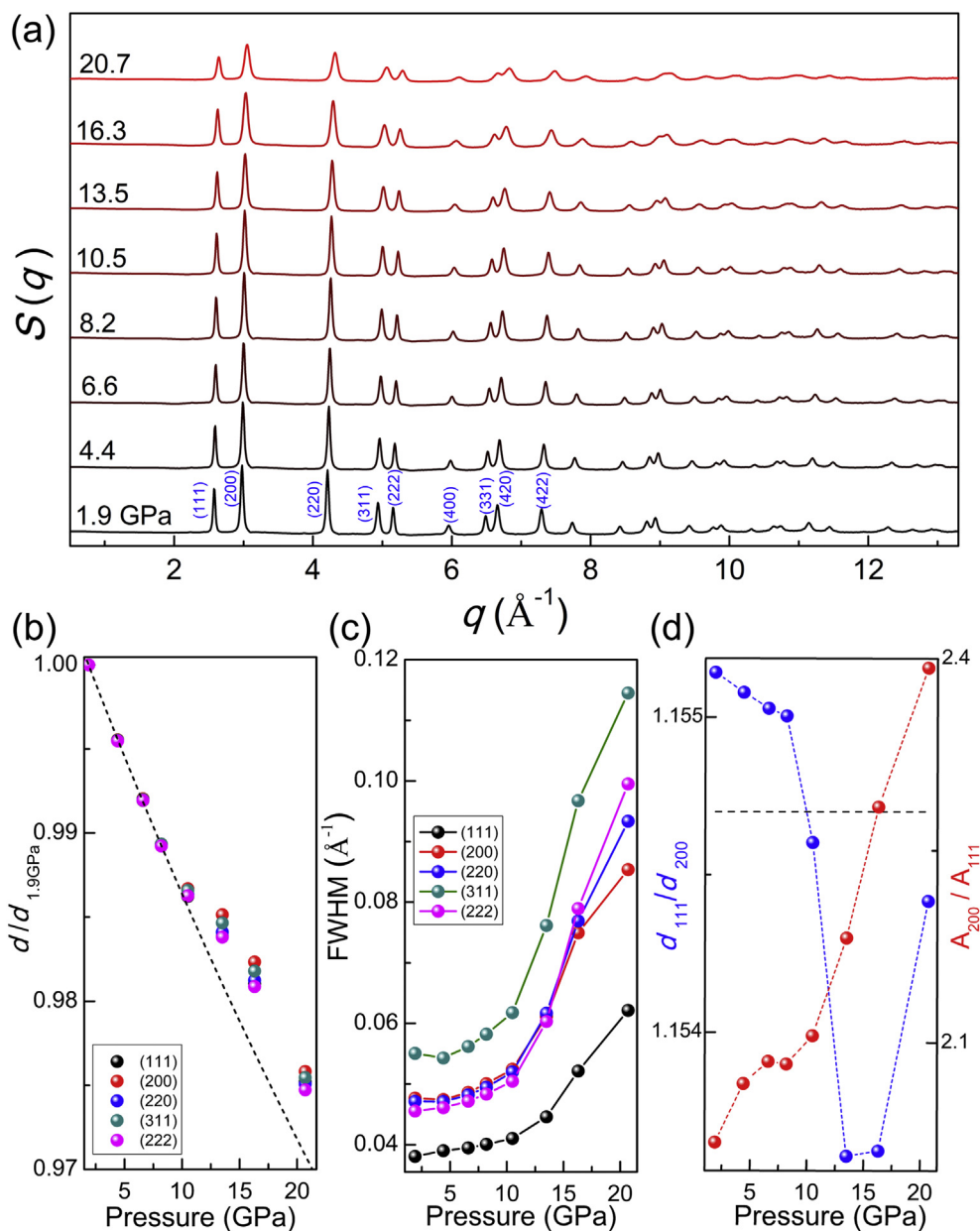


Fig. 2. Structure evolution in reciprocal space of the (Co_{0.2}Cu_{0.2}Mg_{0.2}Ni_{0.2}Zn_{0.2})O TM-HEO during compression at room temperature. (a) Structure factor $S(q)$ of (Co_{0.2}Cu_{0.2}Mg_{0.2}Ni_{0.2}Zn_{0.2})O TM-HEO at different pressures up to 20.7 GPa. Pressure dependence of normalized d -spacing ($d/d_{1.9\text{ GPa}}$) (b) and peak width (c) of different diffraction peaks, and the d -spacing and peak area ratios between (111) and (200) peaks (d). The pressure medium for the experiment was methanol-ethanol (4:1) mixture. The dashed line in (b) is calculated to guide the eyes using the third-order Birch-Murnaghan EOS fitting of the low-pressure data (<9 GPa). The black dashed line in (d) represents the ideal value of d_{111}/d_{200} ratio in the rock salt structure. HEO, high-entropy oxide; EOS, equation of state.

(LBNL), USA and the beamline 15U1, Shanghai Synchrotron Radiation Facility, China. *In situ* high-pressure high-temperature angle-dispersive XRD was conducted using an on-line double-side laser heating system coupled with DACs at the beamline 12.2.2, ALS, LBNL, USA.

2.3. Transmission electron microscopy characterization

The initial and high-pressure recovered TM-HEO powder samples were dispersed in ethyl alcohol and picked up using carbon film-supported copper grids. Transmission electron microscopy

(TEM) experiments were carried out using JEM-2100F field emission electron microscope operating at 200 kV.

2.4. Optical laser Raman spectroscopy measurements

In situ high-pressure Raman spectroscopy measurements were conducted using a Renishaw inVia spectrometer with a 532 nm optical laser excitation. High pressure was generated using a symmetric DAC with a culet size of $\sim 400\ \mu\text{m}$ in diameter. The TM-HEO powder sample was prepressed into a pellet and then loaded into a DAC, along with two tiny ruby balls beside the samples to calibrate pressures. Neon was used as the pressure transmitting medium.

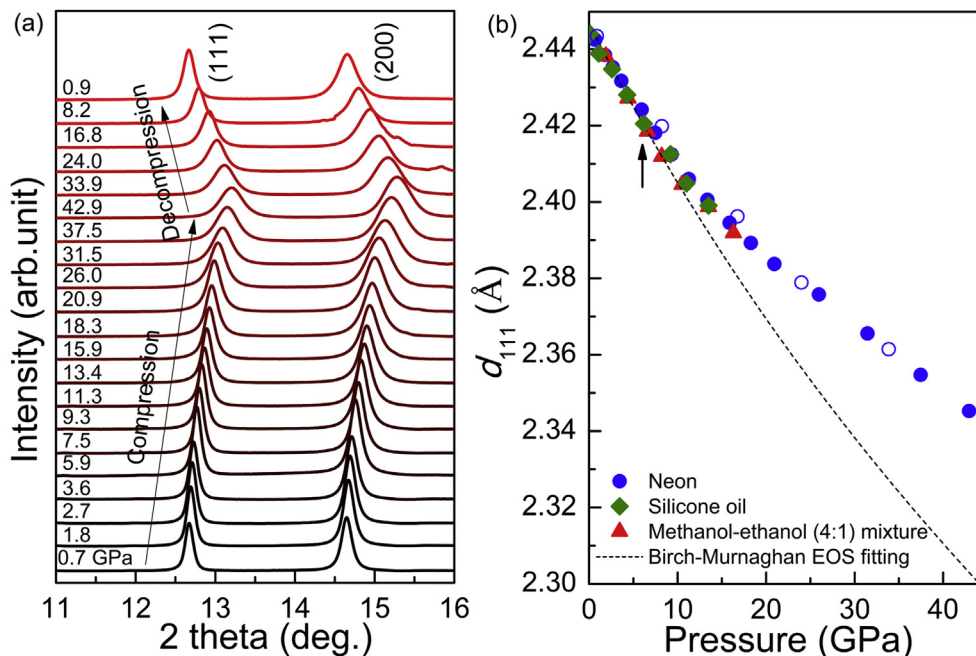


Fig. 3. *In situ* high-pressure XRD measurement of the $(\text{Co}_{0.2}\text{Cu}_{0.2}\text{Mg}_{0.2}\text{Ni}_{0.2}\text{Zn}_{0.2})\text{O}$ TM-HEO in a DAC with neon as the pressure medium. (a) XRD patterns at various pressures during compression and decompression up to 42.9 GPa at room temperature. The X-ray wavelength was 0.3218 Å. (b) Pressure dependence of d -spacing of the (111) peak obtained in experiments with different pressure mediums. The open blue circles are decompression data using neon as the pressure medium. The dashed line in (b) is from the third-order Birch-Murnaghan EOS fitting of the low-pressure data (<9 GPa). HEO, high-entropy oxide; XRD, X-ray diffraction; DACs, diamond anvil cells; EOS, equation of state.

The exposure time for each pattern was ~50 s. The signal from the background was obtained by shining a laser beam on the spot inside the sample chamber but away from the sample.

3. Results and discussion

3.1. Structure of as-prepared sample at ambient conditions

The initial structure of the TM-HEO sample was characterized by synchrotron high-energy XRD. The structure factor $S(q)$ obtained from the high-energy XRD with the moment transfer q coverage up to 30 \AA^{-1} is shown in Fig. 1a. A rock salt type structure with a refined lattice parameter $a = 4.2307(2) \text{ \AA}$ is identified, which is quite consistent with the previous reports [30]. The PDF $G(r)$ shown in Fig. 1b was obtained by a Fourier transformation of the $S(q)$ data after careful background subtraction. By fitting the peaks in $G(r)$, we can determine the bond length and calculate the bond angles accurately. The initial average bond angles of the TM-HEO is very close to the ideal values of a standard rock salt type structure (difference <0.5%), which agrees well with the previous X-ray absorption study [35]. Although there is a quite large difference in ion radii between some constituent cations in the nanocrystalline $(\text{Co}_{0.2}\text{Cu}_{0.2}\text{Mg}_{0.2}\text{Ni}_{0.2}\text{Zn}_{0.2})\text{O}$ TM-HEO, e.g. 0.63 \AA for Ni^{2+} and 0.74 \AA for Zn^{2+} , the average atomic distortion seems much weaker than that in the nanocrystalline rare earth $(\text{Ce}_{0.2}\text{La}_{0.2}\text{Pr}_{0.2}\text{Sm}_{0.2}\text{Y}_{0.2})\text{O}_{2-\delta}$ HEO [14].

3.2. High-pressure synchrotron XRD

Fig. 2a presents the structure factor $S(q)$ of the nanocrystalline $(\text{Co}_{0.2}\text{Cu}_{0.2}\text{Mg}_{0.2}\text{Ni}_{0.2}\text{Zn}_{0.2})\text{O}$ TM-HEO up to ~20 GPa. During compression, the initial rock salt structure seems stable till the highest pressure with no existing Bragg peak disappearing or new peak emerging, whereas the peak intensities weaken and peak

widths broaden obviously. A careful analysis of the peak position, width, and peak area using a Voigt line profile fitting show that a clear change occurs at ~9 GPa. Fig. 2b shows the normalized peak shifting ($d = 2\pi/q$) of different peaks as a function of pressure. Below ~9 GPa, all the peaks shift consistently expected as an isotropic cubic structure. Above ~9 GPa, all the peaks gradually deviate from the initial trend but with a different extent, which indicates the isotropic cubic structure becomes anisotropic and unstable above ~9 GPa. Meanwhile, the peak widths are found to increase rapidly above ~9 GPa. This could be caused by atomic strain/disorder increasing or grain size decreasing. Fig. 2d shows the relative change of the peak position and peak area of (111) to (200). It is demonstrated that the initial crystal structure only slightly deviates from the ideal rock salt structure below ~9 GPa in terms of the ratio of d_{111}/d_{200} , and the deviation sharply decreases and then increases again in the other direction quickly away from the ideal value of 1.1547. The peak area ratio A_{200}/A_{111} exhibits a similar transition zone above ~9 GPa. It should be noted that all the changes or deviations are quite small, only high-quality data could manifest them.

All the abrupt changes occurring at ~9–10 GPa as shown in Fig. 2 happen to overlap with the emerging of non-hydrostaticity of the pressure medium, methanol-ethanol (4:1) mixture [36]. Therefore, to clarify the non-hydrostaticity effect of the pressure medium on the structure change, additional experiments with other pressure mediums were carried out as shown in Fig. 3. Neon could provide good hydrostatic pressure conditions up to ~50 GPa, while silicone oil could ensure relatively good hydrostatic pressure conditions up to ~14 GPa. Moreover, In Fig. 3a, similar behavior with peak intensity weakening and width broadening is observed as in Fig. 2. To look more closely, Fig. 3b shows the d -spacing of (111) peak as a function of pressure compared with other pressure mediums. Within experimental uncertainty, all the data coincide with each other very well up to 16 GPa. It could be concluded that deviation of

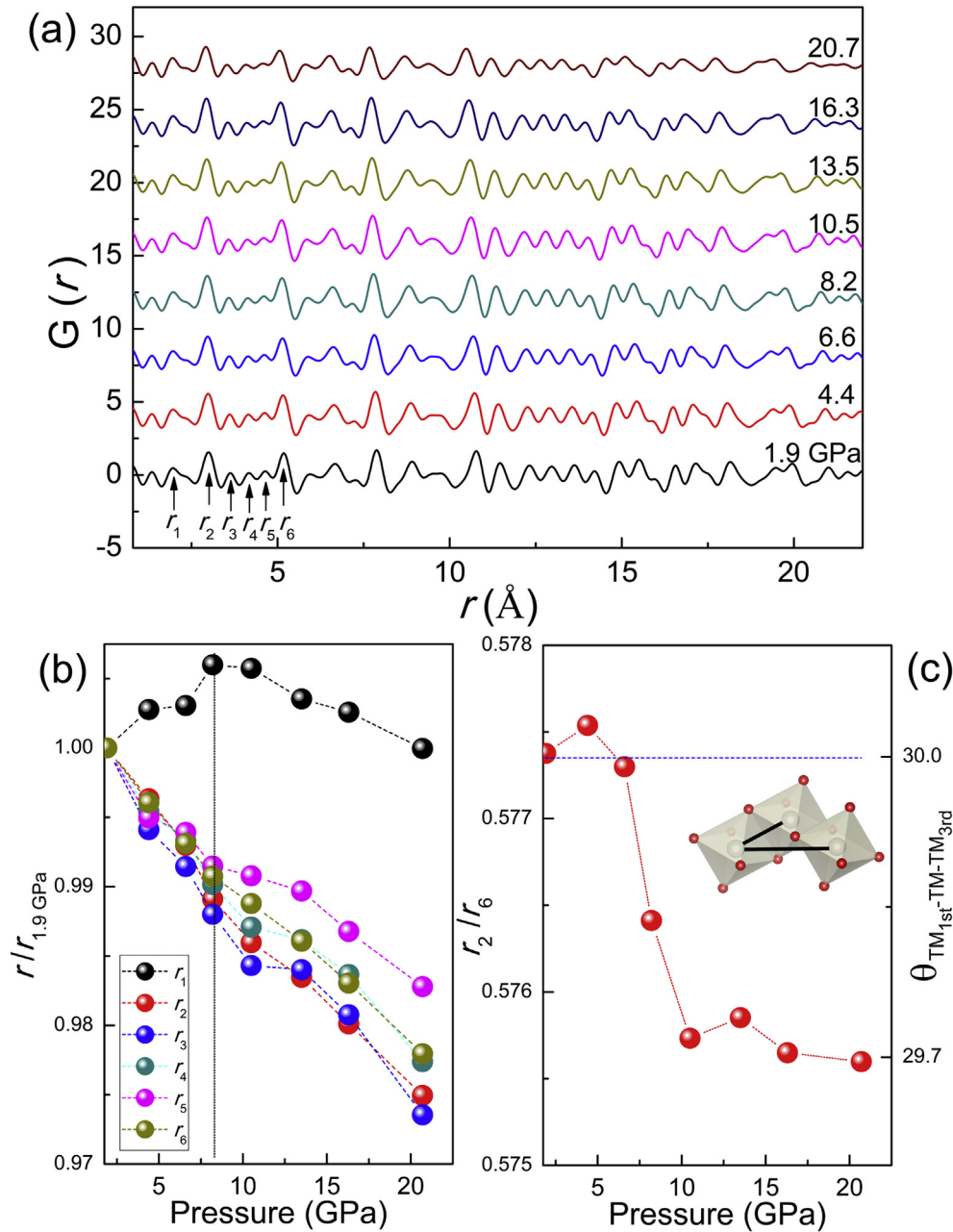


Fig. 4. Structure evolution in real space of the $(\text{Co}_{0.2}\text{Cu}_{0.2}\text{Mg}_{0.2}\text{Ni}_{0.2}\text{Zn}_{0.2})\text{O}$ TM-HEO during compression at room temperature. (a) Pair distribution function of the $(\text{Co}_{0.2}\text{Cu}_{0.2}\text{Mg}_{0.2}\text{Ni}_{0.2}\text{Zn}_{0.2})\text{O}$ TM-HEO at different pressures during compression up to 20.7 GPa. (c) The pressure dependence of the $r/r_{1.9 \text{ GPa}}$ ratio of the first six peaks denoted as r_1 to r_6 in (a). The black dotted line marks the starting pressure of kinks. (d) The pressure dependence of the r_2/r_6 ratio and the bond angle between a TM cation and its second and third TM neighbors. The inset in (d) is a schematic plot of the bond angle. HEO, high-entropy oxide.

the high-pressure data (~ 9 GPa) from the low-pressure data trend (< 9 GPa) could not be attributed to the non-hydrostaticity gradually built up in pressure mediums above ~ 10 GPa. Therefore, the mechanism of the deviation may come from the mechanical stability of the initial rock salt structure of the $(\text{Co}_{0.2}\text{Cu}_{0.2}\text{Mg}_{0.2}\text{Ni}_{0.2}\text{Zn}_{0.2})\text{O}$ TM-HEO. Interestingly, attempts to fit the sample volume as a function of pressure using the third-order Birch-Murnaghan equation of state over pressure ranges beyond ~ 9 GPa produce unreasonably big pressure derivative values, $B'_0 \gg 4$. While fitting the data below ~ 9 GPa yields reasonable results with the bulk modulus $B_0 = 176.1$ GPa and $B'_0 = 3.8$, which further suggests there is a dramatic structural change taking place above

~ 9 GPa. This fitted value of bulk modulus is a little bit smaller than the previously reported value of 187.7 GPa in a bulk sample (grain size of $\sim 10 \mu\text{m}$) [29], which could be attributed to much smaller grain size in this work.

Decompression data was not available for the first *in situ* high-pressure experiment carried out using methanol-ethanol (4:1) mixture, to check the reversibility of the structural change, XRD data were collected during decompression in another later experiment with neon as the pressure medium and much lower x-ray energy (higher resolution in reciprocal space) as shown in Fig. 3. In Fig. 3a, it is obvious that the peak width change is irreversible, and all peaks get permanently broadened after pressure release. In

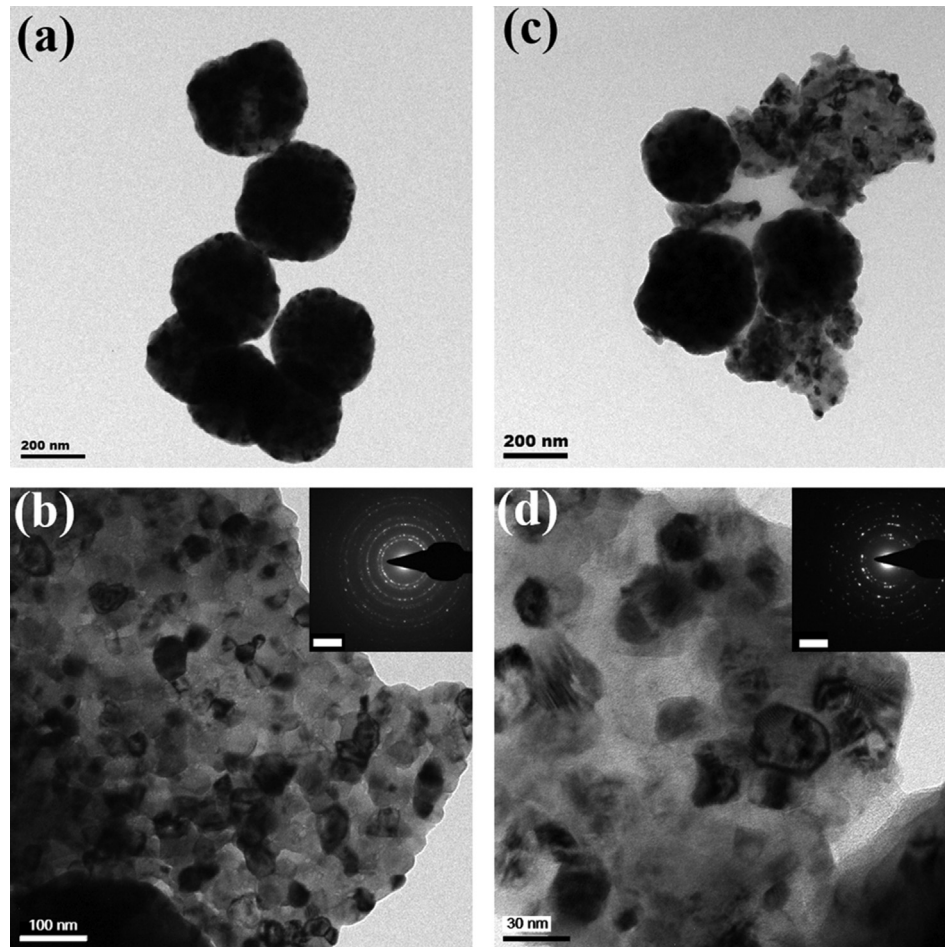


Fig. 5. TEM images and SAED patterns of the initial and high-pressure recovered $(\text{Co}_{0.2}\text{Cu}_{0.2}\text{Mg}_{0.2}\text{Ni}_{0.2}\text{Zn}_{0.2})\text{O}$ TM-HEO samples. Low-magnification TEM images of the initial (a) and high-pressure recovered (c) samples. High-magnification TEM images of the initial (b) and high-pressure recovered (d) samples. The insets in (b) and (d) are SAED patterns, in which the scale bars represent 5 nm^{-1} . HEO, high-entropy oxide; TEM, transmission electron microscopy; SAED, selected area electron diffraction.

contrast, the peak position is basically fully reversible, only showing a small hysteresis from ~ 9 to 15 GPa. The elastic anisotropy and the interplanar d -spacing deviation from low-pressure trend emerging under high pressure typically suggest a second-order phase transition or a weak first-order phase transition. Because a small hysteresis presents during the transition zone, it is most likely a weak first-order rather than second-order phase transition. The irreversible peak width broadening might be mainly caused by a pressure-induced grain refining [37].

3.3. High-pressure PDF analysis in real space

To provide more information of the structural evolution of the $(\text{Co}_{0.2}\text{Cu}_{0.2}\text{Mg}_{0.2}\text{Ni}_{0.2}\text{Zn}_{0.2})\text{O}$ HEO in real space, PDF $G(r)$ was derived from the structure factor $S(q)$ in Fig. 2a after Fourier transformation. It should be noted that although the q coverage in the *in situ* high-pressure XRD measurement is limited ($q_{\text{max}} \approx 14 \text{ \AA}^{-1}$) due to the restricted angular access of DACs; however, the high pressure $S(q)$ and $G(r)$ seem quite reliable in this work in accordance with their consistent feature with the high-energy PDF measurement on the ambient samples ($q_{\text{max}} \approx 30 \text{ \AA}^{-1}$, refer Fig. 1). Fig. 4a shows the $G(r)$ at different pressures up to 20.7 GPa. Peaks in each pattern ($>2 \text{ \AA}$) represent the chance to find another atom at a distance r from a given atom, that is, the distribution of distances between atom pairs. In the rock salt structure of the

$(\text{Co}_{0.2}\text{Cu}_{0.2}\text{Mg}_{0.2}\text{Ni}_{0.2}\text{Zn}_{0.2})\text{O}$ TM-HEO, the TM cations and oxygen anion occupy equal lattice sites. The first six peaks sequentially represent pair distances between the 1st neighbor TM-O, 1st neighbor TM-TM(O-O), 2nd neighbor TM-O, 2nd neighbor TM-TM(O-O), 3rd neighbor TM-O and 3rd neighbor TM-TM(O-O), which are denoted by r_1 , r_2 , r_3 , r_4 , r_5 , and r_6 , respectively. During compression, no existing peak disappears or new peak emerges. This is consistent with the observation in $S(q)$ that there is no obvious phase transition with symmetry breaking. Meanwhile, the peak width and intensity also do not show pronounced change, which means pressure-induced disordering is not a major effect involved during compression.

The rock salt structure of the $(\text{Co}_{0.2}\text{Cu}_{0.2}\text{Mg}_{0.2}\text{Ni}_{0.2}\text{Zn}_{0.2})\text{O}$ TM-HEO consists of TMO_6 octahedrons with an octahedral close-packed arrangement, in which each TM cation is surrounded by six O anions forming six TM-O bonds. All the TMO_6 octahedrons connect with each other by sharing one edge. By fitting the peaks of $G(r)$ using a Voigt line profile, accurate information of the atom pair distances and bond angles can be obtained. Fig. 4b shows the first six atom pairs distances as a function of pressure. The first neighbor TM-O bonds (r_1) inside TMO_6 octahedrons are quite rigid compared with the other longer atom pairs (bonds), which could result in small compressibility of the TMO_6 octahedron unit, whereas all the other longer atomic distances between different TMO_6 octahedrons still decrease considerably with increasing pressure. A pronounced

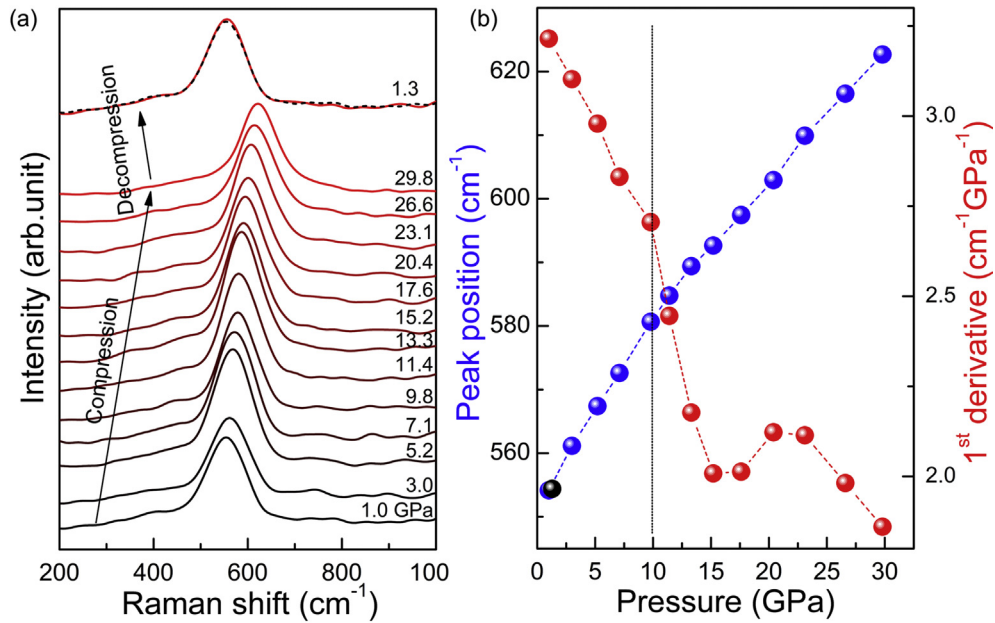


Fig. 6. *In situ* high-pressure Raman spectroscopy measurement. (a) *In situ* high-pressure Raman spectra of the $(\text{Co}_{0.2}\text{Cu}_{0.2}\text{Mg}_{0.2}\text{Ni}_{0.2}\text{Zn}_{0.2})\text{O}$ TM-HEO in a DAC during compression and decompression at room temperature with neon as the pressure medium. (a) Raman spectra upon compression and decompression. The spectrum at 1.3 GPa during decompression fully coincides with the spectrum at 1.0 GPa (dotted) during compression, which indicates the pressure-induced changes in structures are reversible. (b) The pressure dependence of Raman peak positions during compression (blue circles) and decompression (black circle) and the first derivative of the data during compression (red circles). HEO, high-entropy oxide; diamond anvil cells.

transition can be identified by the kinks at ~ 9 GPa in Fig. 4b. Above ~ 9 GPa, relatively, all the atom pairs become less compressible. To further check the stability of the initial rock salt structure, the most intense two peaks, r_2 and r_6 are used to calculate the pair distance

ratio and the bond angle as shown in Fig. 4c. Below ~ 7 GPa or above ~ 10 GPa, r_2/r_6 ratio remains almost constant with a sharp drop in between, which manifests distinct low- and high-pressure states. The r_2/r_6 ratio changes by $\sim 0.3\%$, and the corresponding bond angle

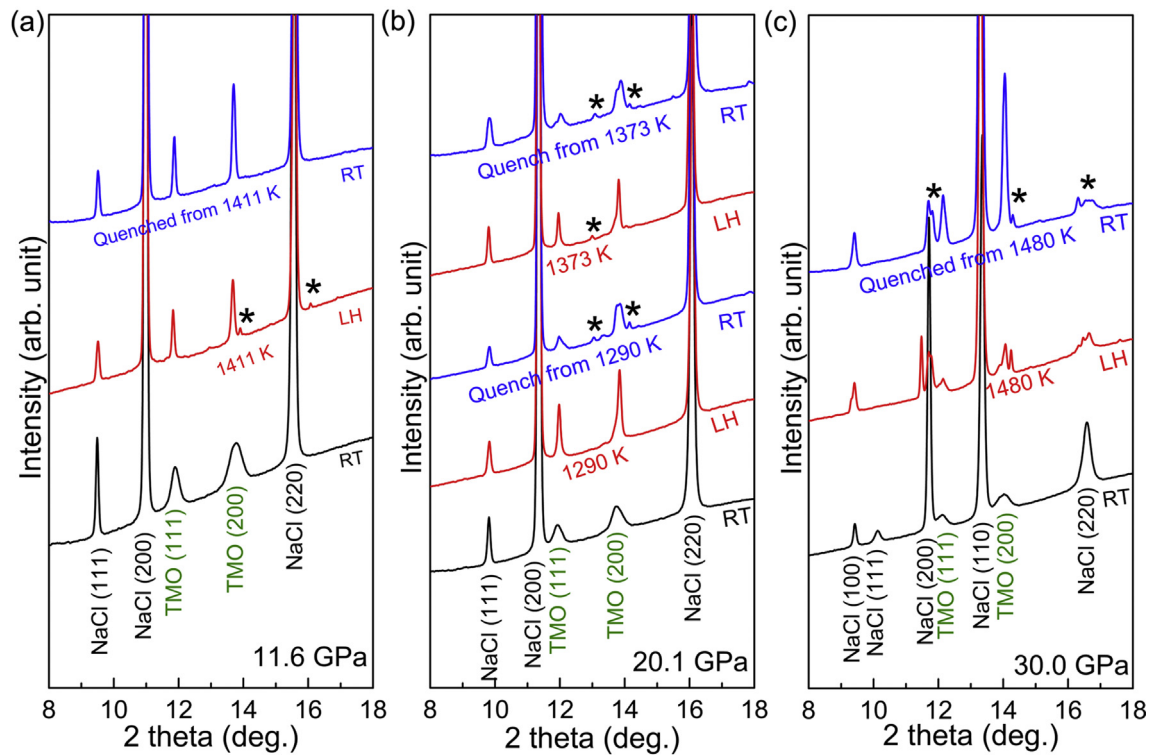


Fig. 7. *In situ* high-pressure synchrotron laser-heating XRD. *In situ* high-pressure synchrotron laser-heating XRD patterns of $(\text{Co}_{0.2}\text{Cu}_{0.2}\text{Mg}_{0.2}\text{Ni}_{0.2}\text{Zn}_{0.2})\text{O}$ TM-HEO in a DAC at 11.6 GPa (a), 20.1 GPa (b), and 30.0 GPa (c). Two heating-quenching cycles were tried at 20.1 GPa. The NaCl was used as a pressure standard and thermal insulator layers. At 30.0 GPa, a phase transition from B1 to B2 structures happens in NaCl. HEO, high-entropy oxide; XRD, X-ray diffraction; diamond anvil cells.

changes by ~1% between the low- and high-pressure states. The sample volume compression could be achieved mainly by bending bonds. However, the distortion caused by the inconsistent compressibilities of different atom pairs and resultant bond bending is still limited even at the highest pressure in this study, not beyond the mechanical instability limit of the initial rock salt structure. It is reasonable to speculate that the high-pressure structure is a highly distorted form of the initial rock salt structure. And the two structures may be linked through a reversible weak first-order phase transition but without symmetry breaking.

3.4. TEM measurements on the initial and high-pressure recovered samples

Because the changes of peak width in XRD patterns are irreversible, TEM measurement was carried out on the initial and high-pressure recovered (compressed to ~30 GPa using neon as the pressure medium) samples (shown in Fig. 5) to clarify the origin of the irreversible XRD peak broadening. It is clear that the particle size has no obvious change; however, in accordance with statistical analysis of tens of grains, the average grain size is 44 ± 3 nm in the initial sample, whereas it is 26 ± 1 nm in the high-pressure recovered sample. The structure in both samples is identified to be the rock salt structure, and no extra diffuse signal from an amorphous structure was observed in the selected area electron diffraction shown as the insets in Fig. 5b and d.

3.5. High-pressure Raman spectroscopy

In the rock salt structure of the $(\text{Co}_{0.2}\text{Cu}_{0.2}\text{Mg}_{0.2}\text{Ni}_{0.2}\text{Zn}_{0.2})\text{O}$ TM-HEO, each TM cation is octahedrally coordinated to six O anion. Therefore, theoretically, the O_h symmetry should lead to the observation of two stretching and one bending Raman active modes (A_{1g} , E_g , and F_{2g}) [38], which could be used as an alternative probe to study the local structure of oxides. Fig. 6a shows the Raman spectra at different pressure during compression and decompression up to ~30 GPa. Only one Raman mode A_{1g} can be observed at 550 cm^{-1} at ambient pressure. This is consistent with the previous report [39]. The disappearance of the other Raman modes is mainly attributed to the cation disorder in HEOs [39,40]. In accordance with the Raman spectra in Fig. 6a, again, no new peak emerges. The peak intensity and width of the Raman peak also do not change obviously with increasing or decreasing pressure. Therefore, no obvious structural symmetry breaking or disordering happens during compression. The Raman peak position shifts to higher frequency as typically observed during compression and the shifting is fully reversible after pressure release. The first-order derivative of the peak position shifting as a function of pressure shows a sharp slope change between ~10 GPa and ~20 GPa. This discontinuous change suggests a structural transition which is consistent with the observation in *in situ* XRD and PDF measurements.

3.6. *In situ* high-pressure synchrotron laser-heating XRD

In accordance with the structural change observed by compression at room temperature, we speculate that the stability of the rock salt phase of $(\text{Co}_{0.2}\text{Cu}_{0.2}\text{Mg}_{0.2}\text{Ni}_{0.2}\text{Zn}_{0.2})\text{O}$ TM-HEO is weakened under high pressure. However, a symmetry-breaking transition is hindered by a high energy barrier. Therefore, we further performed *in situ* laser-heating XRD measurements at three different pressures on the $(\text{Co}_{0.2}\text{Cu}_{0.2}\text{Mg}_{0.2}\text{Ni}_{0.2}\text{Zn}_{0.2})\text{O}$ TM-HEO (as shown in Fig. 7). During heating, the samples at three pressures all have sharper diffraction peaks and the sharper peaks could remain after cooling, which is typical as the grain growth at high

temperatures. Moreover, new peaks emerge during heating for all the studied pressures. After cooling, the new peaks disappear at 11.6 GPa. However, they could remain at 20.1 GPa and 30.0 GPa. Although the new phases that appear at high temperatures could not be resolved due to the limited peaks detected, these results confirm our speculation that the $(\text{Co}_{0.2}\text{Cu}_{0.2}\text{Mg}_{0.2}\text{Ni}_{0.2}\text{Zn}_{0.2})\text{O}$ TM-HEO become unstable at high pressures. The pressure of 11.6 GPa may still be at the boundary between the stable and unstable zones. Therefore, the high-temperature phase could not be quenched to room temperature. This agrees well with the observation in the room temperature XRD experiments discussed previously that the pressure-induced transition starts at ~9–10 GPa.

Phase transitions under high pressure have been extensively studied in all of its constituent transition metal oxides in nano-forms or bulk forms of the TM-HEO. In the pressure range from ambient condition to ~40 GPa covered in our XRD experiments, no phase transition has been observed in tenorite CuO [41], rock salt NiO [42], or rock salt MgO [43], whereas phase transitions exist in CoO from a rock salt cubic phase to a rhombohedral phase at ~43 GPa [44] and exist in ZnO from a wurtzite hexagonal phase to a cubic phase at ~10 GPa [45]. It seems the structural transition in this work is not simply inherited from any of its constituent oxides. In contrast, the development of the local lattice distortion of HEO could play an essential role. The $(\text{Co}_{0.2}\text{Cu}_{0.2}\text{Mg}_{0.2}\text{Ni}_{0.2}\text{Zn}_{0.2})\text{O}$ TM-HEO consists of five cations with different ionic radii and the oxygen sublattice accommodates large disorder [35]. How each specific TM cation and oxygen sublattice behave is interesting; however, the current techniques used in this work could not address it. Element-specific technique such as *in situ* high-pressure extended x-ray absorption fine structure spectroscopy could help to solve this problem, which calls for further efforts in the future.

4. Conclusions

In summary, we studied the structural evolution of the $(\text{Co}_{0.2}\text{Cu}_{0.2}\text{Mg}_{0.2}\text{Ni}_{0.2}\text{Zn}_{0.2})\text{O}$ HEO during compression up to ~40 GPa using *in situ* high-pressure synchrotron XRD and optical Raman spectroscopy. The initial rock salt structure becomes anisotropic and obviously distorted above ~9–10 GPa. PDF analysis reveals that the bonds in the first shell are much more rigid than the other shells, which causes bonds bending and deviation from the ideal values of the standard rock salt structure. Although severe distortion develops with increasing pressure above ~9 GPa, no new peak emerges or existing peaks disappear in the structure factor, PDF, and Raman spectra. Therefore, no traditional symmetry breaking phase transition occurs. Meanwhile, the distortion seems not beyond the mechanical instability limit of the initial rock salt structure; thus, a pressure-induced disordering is not observed. The peak width in structure factor increases with pressure above ~9 GPa and remains broadened after pressure release, while the peak width and intensity in PDF and Raman spectra keep almost constant, which also suggests grain refining rather than structural disordering. Further TEM experiment on the high-pressure recovered samples confirms the grain refining. The results observed in this nanocrystalline $(\text{Co}_{0.2}\text{Cu}_{0.2}\text{Mg}_{0.2}\text{Ni}_{0.2}\text{Zn}_{0.2})\text{O}$ TM-HEO is different from the bulk HEO reported before, which suggests a dramatic size effect in HEOs [46]. Because HEOs may commonly involve local lattice distortion due to cation size mismatch and/or disorder in the oxygen sublattice, pressure-induced structural transitions/tuning may be general in HEOs and is worth more extensive exploration in the future.

Funding

This work was supported by the National Natural Science Foundation of China (No. 51871054, U1930401), the Fundamental Research Funds for the Central Universities, China Postdoctoral Science Foundation (No. 2019M660462), and the Deutsche Forschungsgemeinschaft (DFG) under contract number HH 1344/43-1.

Data availability

The raw/processed data required to reproduce these findings cannot be shared at this time as the data also forms part of an ongoing study.

Declaration of competing interest

The authors declare that they have no known competing financial interests or personal relationships that could have appeared to influence the work reported in this paper.

Acknowledgements

The authors thank Dr. Yanjun Li from Shanghai Institute of Measurement and Testing Technology (SIMT) for her kind help with the TEM measurements and Dr. Yang Ding for helpful discussions. A part of this research was carried out at the beamline P02.2, PETRA-III, DESY, Germany. The authors acknowledge DESY (Hamburg, Germany), a member of the Helmholtz Association HGF, for the provision of experimental facilities. A part of this work used the beamlines 13-ID-D and 16-ID-B of Advanced Photo Source (APS), USA, the beamline 12.2.2, Advanced Light Source (ALS), USA, and also 15U1 of Shanghai Synchrotron Radiation Facility (SSRF), China. ALS is a DOE Office of Science User Facility under contract no. DE-AC02-05CH11231. The usage of the beamline 13-ID-D at APS was supported by the National Science Foundation (NSF)-Earth Sciences (EAR-1634415) and Department of Energy (DOE)-GeoSciences (DE-FG02-94ER14466). APS was supported by the DOE Office of Science (DE-AC02-06CH11357).

References

- [1] J.W. Yeh, S.K. Chen, S.J. Lin, J.Y. Gan, T.S. Chin, T.T. Shun, C.H. Tsau, S.Y. Chang, Nanostructured high-entropy alloys with multiple principal elements: novel alloy design concepts and outcomes, *Adv. Eng. Mater.* 6 (2004) 299–303, <https://doi.org/10.1002/adem.200300567>.
- [2] B. Cantor, I.T.H. Chang, P. Knight, A.J.B. Vincent, Microstructural development in equiatomic multicomponent alloys, *Mater. Sci. Eng., A* 375–377 (2004) 213–218, <https://doi.org/10.1016/j.msea.2003.10.257>.
- [3] S. Singh, N. Wanderka, B.S. Murty, U. Glatzel, J. Banhart, Decomposition in multi-component AlCoCrCuFeNi high-entropy alloy, *Acta Mater.* 59 (2011) 182–190, <https://doi.org/10.1016/j.actamat.2010.09.023>.
- [4] Y. Zhang, X. Yang, P.K. Liaw, Alloy design and properties optimization of high-entropy alloys, *JOM* 64 (2012) 830–838, <https://doi.org/10.1007/s11837-012-0366-5>.
- [5] Y. Zhang, T.T. Zuo, Z. Tang, M.C. Gao, K.A. Dahmen, P.K. Liaw, Z.P. Lu, Microstructures and properties of high-entropy alloys, *Prog. Mater. Sci.* 61 (2014) 1–93, <https://doi.org/10.1016/j.pmatsci.2013.10.001>.
- [6] B.L. Mucicó, D. Gilbert, T.Z. Ward, K. Page, E. George, J. Yan, D. Mandrus, V. Keppens, The emergent field of high entropy oxides: design, prospects, challenges, and opportunities for tailoring material properties, *Apl. Mater.* 8 (2020), 040912, <https://doi.org/10.1063/1.50003149>.
- [7] C.M. Rost, E. Sachet, T. Borman, A. Moballeggh, E.C. Dickey, D. Hou, J.L. Jones, S. Curtarolo, J.P. Maria, Entropy-stabilized oxides, *Nat. Commun.* 6 (2015) 8485, <https://doi.org/10.1038/ncomms9485>.
- [8] R. Djenadic, A. Sarkar, O. Clemens, C. Loh, M. Botros, V.S.K. Chakravadhanula, C. Kübel, S.S. Bhattacharya, A.S. Gandhi, H. Hahn, Multicomponent equiatomic rare earth oxides, *Mater. Res. Lett.* 5 (2016) 102–109, <https://doi.org/10.1080/21663831.2016.1220433>.
- [9] A. Sarkar, R. Djenadic, D. Wang, C. Hein, R. Kautenburger, O. Clemens, H. Hahn, Rare earth and transition metal based entropy stabilised perovskite type oxides, *J. Eur. Ceram. Soc.* 38 (2018) 2318–2327, <https://doi.org/10.1016/j.jeurceramsoc.2017.12.058>.
- [10] S. Jiang, T. Hu, J. Gild, N. Zhou, J. Nie, M. Qin, T. Harrington, K. Vecchio, J. Luo, A new class of high-entropy perovskite oxides, *Scripta Mater.* 142 (2018) 116–120, <https://doi.org/10.1016/j.scriptamat.2017.08.040>.
- [11] F. Okejiri, Z. Zhang, J. Liu, M. Liu, S. Yang, S. Dai, Room-temperature synthesis of high-entropy perovskite oxide nanoparticle catalysts through ultrasonication-based method, *ChemSusChem* 13 (2020) 111–115, <https://doi.org/10.1002/cssc.201902705>.
- [12] J. Dąbrowa, M. Stygar, A. Mikula, A. Knapik, K. Mroczka, W. Tejchman, M. Danielewski, M. Martin, Synthesis and microstructure of the (Co,Cr,Fe,Mn,Ni) 3 O 4 high entropy oxide characterized by spinel structure, *Mater. Lett.* 216 (2018) 32–36, <https://doi.org/10.1016/j.matlet.2017.12.148>.
- [13] J. Zhang, X. Zhang, Y. Li, Q. Du, X. Liu, X. Qi, High-entropy oxides 10La2O3-20TiO2-10Nb2O5-20WO3-20ZrO2 amorphous spheres prepared by containerless solidification, *Mater. Lett.* 244 (2019) 167–170, <https://doi.org/10.1016/j.matlet.2019.01.017>.
- [14] B. Cheng, H. Lou, A. Sarkar, Z. Zeng, F. Zhang, X. Chen, L. Tan, V. Prakapenka, E. Greenberg, J. Wen, R. Djenadic, H. Hahn, Q. Zeng, Pressure-induced tuning of lattice distortion in a high-entropy oxide, *Comm. Chem.* 2 (2019) 114, <https://doi.org/10.1038/s42004-019-0216-2>.
- [15] D. Bérandan, S. Franger, D. Dragoe, A.K. Meena, N. Dragoe, Colossal dielectric constant in high entropy oxides, *Phys. Status Solidi RRL* 10 (2016) 328–333, <https://doi.org/10.1002/pssr.201600043>.
- [16] D. Bérandan, S. Franger, A.K. Meena, N. Dragoe, Room temperature lithium superionic conductivity in high entropy oxides, *J. Mater. Chem.* 4 (2016) 9536–9541, <https://doi.org/10.1039/c6ta03249d>.
- [17] W. Hu, Y. Liu, R.L. Withers, T.J. Frankcombe, L. Norén, A. Snashall, M. Kitchin, P. Smith, B. Gong, H. Chen, J. Schiemer, F. Brink, J. Wong-Leung, Electron-pinned defect-dipoles for high-performance colossal permittivity materials, *Nat. Mater.* 12 (2013) 821, <https://doi.org/10.1038/nmat3691>.
- [18] C.M. Rost, Entropy-Stabilized Oxides: Explorations of a Novel Class of Multi-component Materials, Doctor of Philosophy, North Carolina State University, 2016.
- [19] A. Sarkar, L. Velasco, D. Wang, Q. Wang, G. Talasila, L. de Biasi, C. Kubel, T. Brezesinski, S.S. Bhattacharya, H. Hahn, B. Breitung, High entropy oxides for reversible energy storage, *Nat. Commun.* 9 (2018) 3400, <https://doi.org/10.1038/s41467-018-05774-5>.
- [20] N. Qiu, H. Chen, Z. Yang, S. Sun, Y. Wang, Y. Cui, A high entropy oxide (Mg0.2Co0.2Ni0.2Cu0.2Zn0.2O) with superior lithium storage performance, *J. Alloys Compd.* 777 (2019) 767–774, <https://doi.org/10.1016/j.jallcom.2018.11.049>.
- [21] C.L. Tracy, S. Park, D.R. Rittman, S.J. Zinkle, H. Bei, M. Lang, R.C. Ewing, W.L. Mao, High pressure synthesis of a hexagonal close-packed phase of the high-entropy alloy CrMnFeCoNi, *Nat. Commun.* 8 (2017) 15634, <https://doi.org/10.1038/ncomms15634>.
- [22] E.W. Huang, C.-M. Lin, J. Jain, S.R. Shieh, C.-P. Wang, Y.-C. Chuang, Y.-F. Liao, D.-Z. Zhang, T. Huang, T.-N. Lam, W. Woo, S.Y. Lee, Irreversible phase transformation in a CoCrFeMnNi high entropy alloy under hydrostatic compression, *Mater. Today Commun.* 14 (2018) 10–14, <https://doi.org/10.1016/j.mtcomm.2017.12.001>.
- [23] F. Zhang, Y. Wu, H. Lou, Z. Zeng, V.B. Prakapenka, E. Greenberg, Y. Ren, J. Yan, J.S. Okasinski, X. Liu, Y. Liu, Q. Zeng, Z. Lu, Polymorphism in a high-entropy alloy, *Nat. Commun.* 8 (2017) 15687, <https://doi.org/10.1038/ncomms15687>.
- [24] F.X. Zhang, S. Zhao, K. Jin, H. Bei, D. Popov, C. Park, J.C. Neuefeind, W.J. Weber, Y. Zhang, Pressure-induced fcc to hcp phase transition in Ni-based high entropy solid solution alloys, *Appl. Phys. Lett.* 110 (2017), 011902, <https://doi.org/10.1063/1.4973627>.
- [25] P.F. Yu, L.J. Zhang, J.L. Ning, M.Z. Ma, X.Y. Zhang, Y.C. Li, P.K. Liaw, G. Li, R.P. Liu, Pressure-induced phase transitions in HoDyYGdTb high-entropy alloy, *Mater. Lett.* 196 (2017) 137–140, <https://doi.org/10.1016/j.matlet.2017.02.136>.
- [26] B. Cheng, F. Zhang, H. Lou, X. Chen, P.K. Liaw, J. Yan, Z. Zeng, Y. Ding, Q. Zeng, Pressure-induced phase transition in the AlCoCrFeNi high-entropy alloy, *Scripta Mater.* 161 (2019) 88–92, <https://doi.org/10.1016/j.scriptamat.2018.10.020>.
- [27] L. Wang, F. Zhang, Z. Nie, L. Wang, F. Wang, B. Wang, S. Zhou, Y. Xue, B. Cheng, H. Lou, X. Chen, Y. Ren, D.E. Brown, V. Prakapenka, E. Greenberg, Z. Zeng, Q.S. Zeng, Abundant polymorphic transitions in the Al0.6CoCrFeNi high-entropy alloy, *Mater. Today Phys.* 8 (2019) 1–9, <https://doi.org/10.1016/j.mtphys.2018.12.002>.
- [28] F. Zhang, H.B. Lou, B.Y. Cheng, Z.D. Zeng, Q.S. Zeng, High-pressure induced phase transitions in high-entropy alloys: a review, *Entropy* 21 (2019), <https://doi.org/10.3390/e21030239>.
- [29] J. Chen, W. Liu, J. Liu, X. Zhang, M. Yuan, Y. Zhao, J. Yan, M. Hou, J. Yan, M. Kunz, N. Tamura, H. Zhang, Z. Yin, Stability and compressibility of cation-doped high-entropy oxide MgCoNiCuZnO5, *J. Phys. Chem. C* 123 (2019) 17735–17744, <https://doi.org/10.1021/acs.jpcc.9b04992>.
- [30] A. Sarkar, R. Djenadic, N.J. Usharani, K.P. Sanghvi, V.S.K. Chakravadhanula, A.S. Gandhi, H. Hahn, S.S. Bhattacharya, Nanocrystalline multicomponent entropy stabilised transition metal oxides, *J. Eur. Ceram. Soc.* 37 (2017) 747–754, <https://doi.org/10.1016/j.jeurceramsoc.2016.09.018>.
- [31] H.-P. Liermann, Z. Konopkova, W. Morgenroth, K. Glazyrin, J. Bednarcik, E.E. McBride, S. Petitgirard, J.T. Delitz, M. Wendt, Y. Bican, A. Ehnés, I. Schwark, A. Rothkirch, M. Tischer, J. Heuer, H. Schulte-Schrepping, T. Kracht, H. Franz, The extreme conditions beamline P02.2 and the extreme conditions science infrastructure at PETRA III, *J. Synchrotron Radiat.* 22 (2015) 908–924, <https://doi.org/10.1107/S1600577515005937>.

- [32] H.-K. Mao, B. Chen, J. Chen, K. Li, J.-F. Lin, W. Yang, H. Zheng, Recent advances in high-pressure science and technology, *Matter Radiat. Extr.* 1 (2016) 59–75, <https://doi.org/10.1016/j.mre.2016.01.005>.
- [33] C. Prescher, V.B. Prakapenka, DIOPTAS: a program for reduction of two-dimensional X-ray diffraction data and data exploration, *High Pres. Res.* 35 (2015) 223–230, <https://doi.org/10.1080/08957959.2015.1059835>.
- [34] P. Juhas, T. Davis, C.L. Farrow, S.J.L. Billinge, PDFgetX3: a rapid and highly automatable program for processing powder diffraction data into total scattering pair distribution functions, *J. Appl. Crystallogr.* 46 (2013) 560–566, <https://doi.org/10.1107/S0021889813005190>.
- [35] C.M. Rost, Z. Rak, D.W. Brenner, J.-P. Maria, Local structure of the $\text{Mg}_x\text{Ni}_x\text{Co}_x\text{Cu}_x\text{Zn}_x\text{O}(x=0.2)$ entropy-stabilized oxide: an EXAFS study, *J. Am. Ceram. Soc.* 100 (2017) 2732–2738, <https://doi.org/10.1111/jace.14756>.
- [36] S. Klotz, J.C. Chervin, P. Munsch, G. Le Marchand, Hydrostatic limits of 11 pressure transmitting media, *J. Phys. D Appl. Phys.* 42 (2009), 075413, <https://doi.org/10.1088/0022-3727/42/7/075413>.
- [37] V.B. Prakapenka, G. Shen, M.L. Rivers, S.R. Sutton, L. Dubrovinsky, Grain-size control in situ at high pressures and high temperatures in a diamond-anvil cell, *J. Synchrotron Radiat.* 12 (2005) 560–565, <https://doi.org/10.1107/S0909049505021928>.
- [38] D. Gallant, M. Pézolet, S. Simard, Optical and physical properties of cobalt oxide films electrogenerated in bicarbonate aqueous media, *J. Phys. Chem. B* 110 (2006) 6871–6880, <https://doi.org/10.1021/jp056689h>.
- [39] J. Dąbrowa, M. Stygar, A. Mikula, A. Knapik, K. Mrocza, W. Tejchman, M. Danielewski, M. Martin, Synthesis and microstructure of the $(\text{Co,Cr,Fe,Mn,Ni})_3\text{O}_4$ high entropy oxide characterized by spinel structure, *Mater. Lett.* 216 (2018) 32–36, <https://doi.org/10.1016/j.matlet.2017.12.148>.
- [40] A. Sarkar, C. Loho, L. Velasco, T. Thomas, S.S. Bhattacharya, H. Hahn, R. Djenadic, Multicomponent equiatomic rare earth oxides with a narrow band gap and associated praseodymium multivalency, *Dalton Trans.* 46 (2017) 12167–12176, <https://doi.org/10.1039/C7DT02077E>.
- [41] Z. Wang, V. Pischedda, S.K. Saxena, P. Lazor, X-ray diffraction and Raman spectroscopic study of nanocrystalline CuO under pressures, *Solid State Commun.* 121 (2002) 275–279, [https://doi.org/10.1016/S0038-1098\(01\)00509-9](https://doi.org/10.1016/S0038-1098(01)00509-9).
- [42] T. Eto, S. Endo, M. Imai, Y. Katayama, T. Kikegawa, Crystal structure of NiO under high pressure, *Phys. Rev. B* 61 (2000) 14984–14988, <https://doi.org/10.1103/PhysRevB.61.14984>.
- [43] T.S. Duffy, R.J. Hemley, H. Mao, Equation of state and shear strength at multimegabar pressures: magnesium oxide to 227 GPa, *Phys. Rev. Lett.* 74 (1995) 1371–1374, <https://doi.org/10.1103/PhysRevLett.74.1371>.
- [44] Q. Guo, H.-K. Mao, J. Hu, J. Shu, R.J. Hemley, The phase transitions of CoO under static pressure to 104 GPa, *J. Phys. Condens. Matter* 14 (2002) 11369–11374, <https://doi.org/10.1088/0953-8984/14/44/484>.
- [45] B. Cheng, Q. Li, M. Yao, R. Liu, D. Li, B. Zou, T. Cui, J. Liu, Z. Chen, Z. Zhao, B. Yang, B. Liu, High pressure phase transition of ZnO/SiO₂ core/shell nanospheres, *J. Appl. Phys.* 113 (2013), <https://doi.org/10.1063/1.4790702>.
- [46] A.D. Dupuy, X. Wang, J.M. Schoenung, Entropic phase transformation in nanocrystalline high entropy oxides, *Mater. Res. Lett.* 7 (2019) 60–67, <https://doi.org/10.1080/21663831.2018.1554605>.